AFRL-OSR-VA-TR-2014-0101

PROTECTING SUPERCONDUCTING HTS-ANTENNAS BY META-MATERIAL CLOAKS

Horst Rogalla
REGENTS OF THE UNIVERSITY OF COLORADO THE

04/30/2014
Final Report

Air Force Research Laboratory
AF Office Of Scientific Research (AFOSR)/ RTD
Arlington, Virginia 22203
Air Force Materiel Command

REPORT DOCUMENTATION PAGE

Form Approved
OMB No. 0704-0188

1. REPORT DATE *(DD-MM-YYYY)*	**2. REPORT TYPE**	**3. DATES COVERED** *(From - To)*
06-04-2014	Final Report	01-08-2010 till 31-01-2014

4. TITLE AND SUBTITLE

Protecting Superconducting HTS-Antennas by Meta-Material Cloaks

5a. CONTRACT NUMBER

FA9550-10-1-0413

5b. GRANT NUMBER

5c. PROGRAM ELEMENT NUMBER

6. AUTHOR(S)

Horst Rogalla, Frank Trang, Zoya Popović

5d. PROJECT NUMBER

5e. TASK NUMBER

5f. WORK UNIT NUMBER

7. PERFORMING ORGANIZATION NAME(S) AND ADDRESS(ES)

Regents of the University of Colorado
The Office of Contracts and Grants
3100 Marine St 572 UCB
Boulder CO 80309-0001

8. PERFORMING ORGANIZATION REPORT NUMBER

9. SPONSORING / MONITORING AGENCY NAME(S) AND ADDRESS(ES)

Dr. Harold Weinstock
USAF, AFRL DUNS 143574726
AF Office of Scientific Research
875 N. Randolph St. Room 3112
Arlington VA 22203

10. SPONSOR/MONITOR'S ACRONYM(S)

USAF AFRL

11. SPONSOR/MONITOR'S REPORT NUMBER(S)

12. DISTRIBUTION / AVAILABILITY STATEMENT

Approved for Public Release

13. SUPPLEMENTARY NOTES

14. ABSTRACT

This work addresses analysis and design of a cryogenic microwave anisotropic wave guiding structure that isolates an antenna from external incident fields from specific directions. The focus of this research is to design and optimize the radome's constituent material parameters for maximizing the isolation between an interior receiver antenna and an exterior transmitter without significantly disturbing the transmitter antenna far field characteristics.

Meta-material elements (YBCO split-ring resonators on MgO substrate) are optimized to improve the narrowband performance of the meta-material radome with respect to maximizing isolation and minimizing shadowing, defined as a reduction of the transmitted power external to the radome. At 11.12 GHz, measurements show that the HTS metamaterial radome achieved an isolation of 10.5 dB and the external power at 100 mm behind the radome is reduced by only 1.9 dB. This work demonstrates the feasibility of fabricating a structure that provides good isolation between two antennas and low disturbance of the transmitter's fields.I

15. SUBJECT TERMS

Superconductivity, meta-materials, cloaks, microwave antennas, split-ring resonators, YBCO

16. SECURITY CLASSIFICATION OF:			**17. LIMITATION OF ABSTRACT**	**18. NUMBER OF PAGES**	**19a. NAME OF RESPONSIBLE PERSON**
					Horst Rogalla
a. REPORT	**b. ABSTRACT**	**c. THIS PAGE**	UU	22	**19b. TELEPHONE NUMBER** *(include area code)*
U	U	U			303 498 4419

Subject: Final Report to Dr. Harold Weinstock (AFOSR)
Contract/Grant Title: Protecting Superconducting HTS-Antennas by Meta-Material Cloaks
Contract/Grant #: FA9550-10-1-0413
Reporting Period: 1 Aug 2010 to 31 Jan 2014

Protecting Superconducting HTS-Antennas by Meta-Material Cloaks

Frank Trang[1], Horst Rogalla[1, 2], and Zoya Popović[1]
[1]Dept.of ECEE, University of Colorado, Boulder, CO
[2]National Institute of Standards and Technology, Boulder, CO

Abstract

This project addressed the analysis and design of a cryogenic microwave anisotropic wave guiding structure that isolates an antenna from external incident fields from specific directions. The focus of this research was to design and optimize the radome's constituent material parameters for maximizing the isolation between an interior receiver antenna and an exterior transmitter without significantly disturbing the transmitter antenna far field characteristics.

The design, characterization, and optimization of high-temperature superconducting metamaterials constitutive parameters are developed in this work at X-band frequencies. A calibrated characterization method for testing arrays of split-ring resonators at cryogenic temperature inside a TE10 waveguide was developed and used to back-out anisotropic equivalent material parameters. The artificial material elements (YBCO split-ring resonators on MgO substrate) are optimized to improve the narrowband performance of the metamaterial radome with respect to maximizing isolation and minimizing shadowing, defined as a reduction of the transmitted power external to the radome. The optimized radome is fabricated and characterized in a parallel plate waveguide in a cryogenic environment to demonstrate the degree of isolation and shadowing resulting from its presence. At 11.12 GHz, measurements show that the HTS metamaterial radome achieved an isolation of 10.5 dB and the external power at 100 mm behind the radome is reduced by 1.9 dB. This work demonstrates the feasibility of fabricating a structure that provides good isolation between two antennas and low disturbance of the transmitter's fields.

Introduction

This work presents a microwave cryogenic wave guiding structure that provides isolation between an interior receiver and an exterior transmitter without significantly distorting the transmitter antenna far field pattern. A sketch illustrating the problem and approach is shown in Frig. 1 . An arbitrarily-polarized transmitting antenna polarized is able to communicate with an intended receiver some distance away from the isolation structure, minimally affected by its presence. In the figure, the antenna at the center is shown as cross-polarized with respect to the transmitting antenna, which means there is already isolation between the two. However, some power could be coupled into the center antenna. In our

measurements and simulations, these two antennas are co-polarized to simulate the worst case. We will show that isolation can be achieved even in the co-polarized scenario. Small antennas can be made in superconducting technology for improved gain and low noise amplifiers can be cooled for improving the noise figure. This means that the wave guiding radome can also be implemented in superconducting technology, resulting in low loss. It will be shown that a radome that meets the operating requirements has electromagnetic properties that are not found in natural materials. Thus, it will be constructed of metamaterial elements, such as split-ring resonators. The structure is multi-layered and cylindrical in shape, with each layer constructed from arrays of high-temperature superconducting split-ring resonator metamaterials, artificial materials that have properties that are not found in regular materials.

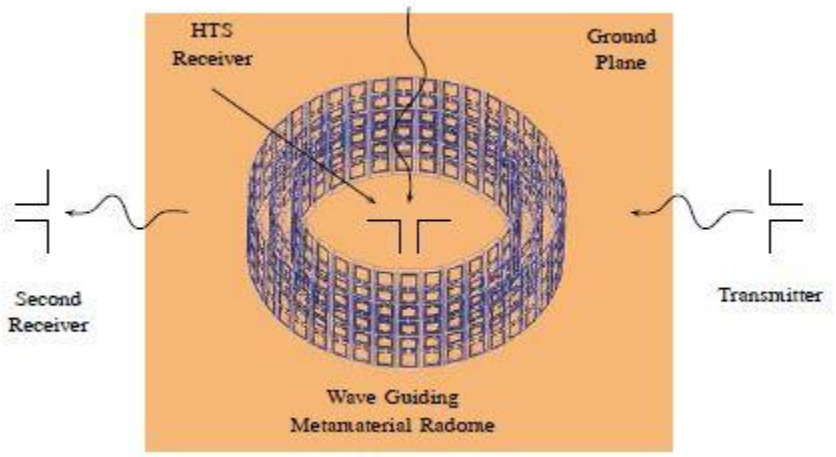

Figure 1: A superconducting receiver antenna is located inside the isolation metamaterial radome in the path of a pair of antennas and is receiving radiation in the zenith direction undisturbed by the other two antennas. The communication link between the pair of dipole antennas (left and right) is unaffected by the radome.

To understand the functionality of the structure, imagine a plane wave propagating in free space with no object in its path. See Figure 2a, where the gray region shows the placement location of the structure. The straight arrows show the direction of the Poynting vector field lines. When the isolation radome is placed in the path of propagation (gray region in Figure 2b), the structure isolates its interior from the outside fields, while outside of the radome the fields are not altered. Such structures have been demonstrated in simulations [1-3] and similar “metamaterial cloaking'' structures have been constructed and measured using normal conducting resonant elements [4,5]. The structure in [4] has properties such that the permeability is radially varying and is measured inside a parallel plate waveguide. The structure in [5] has a radially varying permittivity and is measured in free space (anechoic chamber). In both cases, the amount of isolation in the interior of the cloak and field distortion exterior to the cloak are not quantified. Thus, one can only visually judge the performance of the cloaking ability of the structure. In this project, a probe measures the received power of the measurement environment with and without the wave guiding radome. This gives us the information to quantify the isolation and shadowing characteristics of the structure. Shadowing is defined as a reduction of external transmitted power in the presence of the radome with respect to the no-radome case. Using a cylindrical shape has the advantage that it can be opened on the ends to allows an antenna to be placed in its interior to receive and transmit radiation in the perpendicular direction. For our work,

only the guiding structure has to operate at the same frequency as the transmitter. The receiver can operate at any frequency.

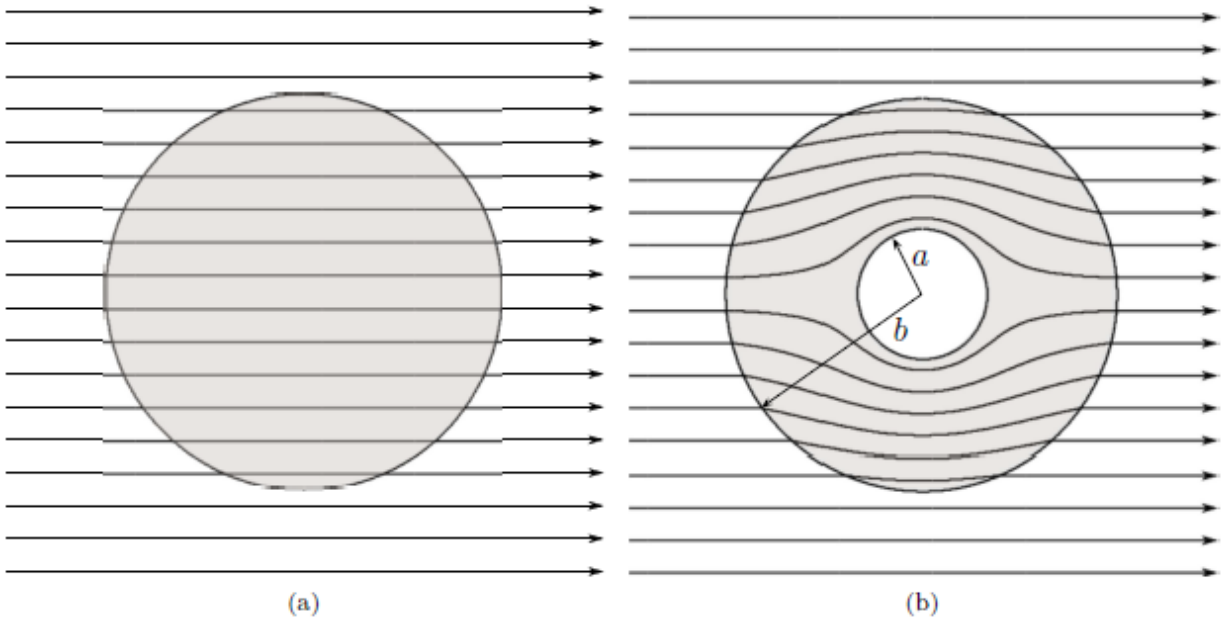

Figure 2: (a) and (b) show the direction of the Poynting vector field lines. In (a) no object is placed in its path. In (b) a cylindrical electromagnetic cloak is placed in the path of the power flow. The interior is completely isolated from the exterior. In addition, the lines are undisturbed outside of the structure.

For small antennas, the loss resistance, R_L, in the conductor and substrate can dominate the radiation impedance, since the real resistance R_r is small. The radiation efficiency given by

$$\eta = \frac{R_r}{R_r + R_L}$$

will therefore be small. To demonstrate the impact loss has on the radiation efficiency, consider an electrically small single copper loop antenna, with diameter d=10 mm and wire radius b=0.5mm. Generally, an antenna is considered electrically small if its largest dimension is less than or equal to one-tenth of the operating wavelength (≤ λ/10). For example, the largest dimensions for a dipole, a loop, and a microstrip patch antenna are the length, diameter, and diagonal, respectively [6]. The radiation resistance R_r and loss resistance R_L for a loop antenna at 1GHz are given by [7]:

$$R_r = 20\pi^2 \left(\frac{\pi d}{\lambda}\right)^4 = 0.0237\,\Omega$$

$$R_L = \frac{l}{P} R_S = \frac{\pi d}{2\pi b}\sqrt{\frac{\omega\mu_0}{2\sigma}} = 0.0825\,\Omega$$

The term R_L represents the loss resistance due to the conductor and dielectric loss, which is almost four times greater than R_r. The antenna radiation efficiency for this antenna is 22.3\%. However, if the

normal conducting part is replaced with a superconductor, e.g. YBCO with R_S=500μΩ, [8] the loss resistance can be brought down due to the much lower surface resistance of the superconductor relative to the normal conductor. Chalupka *et al.* [9] experimentally demonstrated a large increase in radiation efficiency by comparing a miniature copper patch antenna (6mm by 6mm on a 1mm thick substrate) to a high-temperature superconducting (HTS) YBCO-version at 2.45GHz. At 77K the measured efficiency was 3% for the copper patch and 45% for the YBCO patch. The increase in radiation efficiency from copper- to HTS-antennas has also been reported in other literature (see e.g. [10] and [11]).

A disadvantage of superconducting antennas is the need to cool them. In 1986, Bednorz and Müller discovered that LBCO has a T_C in the 30K range [12]. In 1987, Wu *et al.* [13] discovered the HTS compound YBCO that has a T_C of ≈ 92K, which was the first superconductor to have a T_C greater than the boiling temperature of liquid nitrogen. Thus antennas made of high-T_C superconductors can easily be cooled to below T_C with LN_2 (with a boiling temperature of ≈77K) or by a small cryocooler, e.g. from SunPower, Inc. [14], which was used in this project.

Another problem superconducting antennas face is nonlinearity when a strong microwave field creates a surface current density that is comparable to the superconductor J_C (≈ 2MA/cm^2 at 77K). Using the HTS antenna as a transmitter, Chalupka [9] measured a drop in $|S_{21}|/|S_{21}^{max}|$, from unity at -20dBm input power into the feed to ≈ 0.4 at 0dBm input power. Such an antenna would be rendered unusable as a receiver in the presence of a strong transmitter.

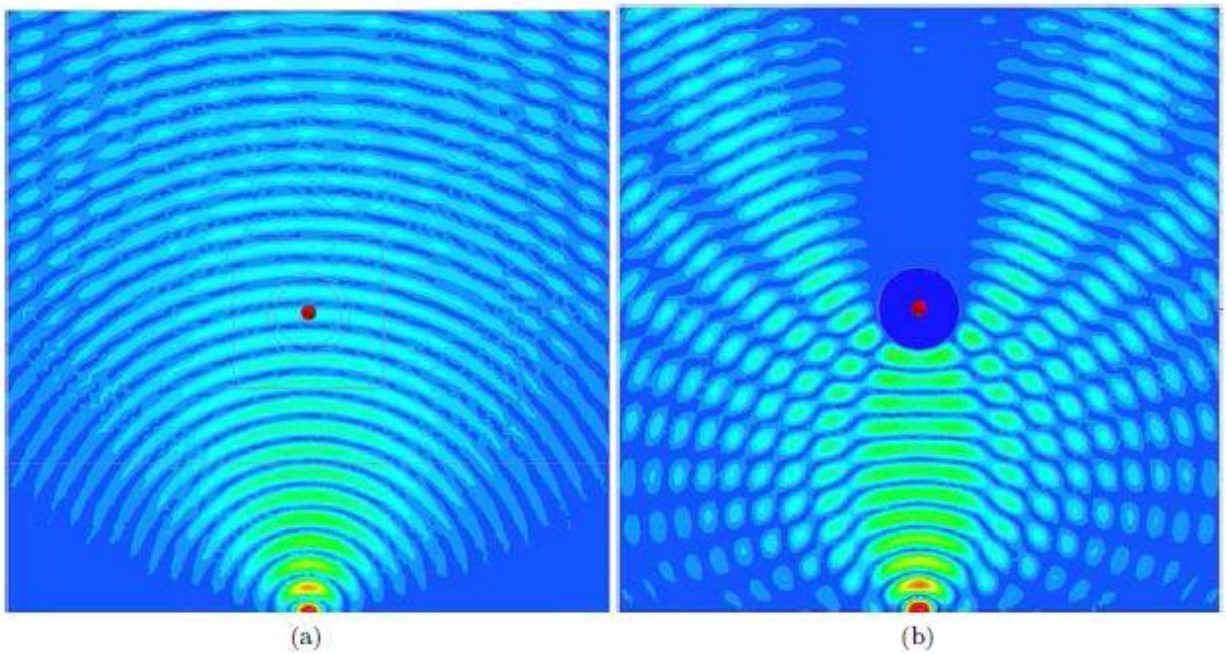

Figure 3: {Electric field plot of (a) an empty parallel plate waveguide and (b) a parallel plate waveguide with a copper cylinder placed some distance away. The E-field is greatly distorted by the presence of the copper cylinder.

One method for isolating the receiver from a transmitter is by shielding them with a copper cylinder. The isolation in this case will be nearly perfect. However, this will greatly alter the transmitter's field

characteristics. Figure 3a shows a snapshot in time of the electric field inside an empty parallel plate waveguide at 9.5GHz. The field plots are generated in the Ansys HFSS full-wave simulation where the source is a waveport excitation (center bottom). The four sides of the waveguide are assigned radiation boundaries to reduce reflection. To illustrate the field distortion in the presence of the copper cylinder, a 1mm thick cylindrical copper shell is placed in the radiation path, Figure 3b. The electric field amplitude is greatly reduced behind the copper shell, in addition to reflection on the transmitter side. An improved approach is to utilize a structure constructed of artificial materials to help guide the EM waves around the receiver. This approach was used in this project and was extensively investigated.

Metamaterials

A metamaterial radome has very specific frequency dependent electromagnetic properties that are not found in homogeneous natural materials. Metamaterials, as defined by Ramakrishna and Grzegorczyk [17], are "composite materials consisting of structural units much smaller than the wavelength of the incident radiation and displaying properties not found in natural materials." In the limit when the dimension of the structural unit is << λ/10 of the incident radiation, the composite material can be treated as having effective homogeneous material parameters [18]. All materials can be mapped into one of the four quadrants described by their electric permittivity, $\varepsilon = \varepsilon' - j\varepsilon''$, and magnetic permeability, $\mu = \mu' - j\mu''$. Materials in quadrant I have both positive permittivity and permeability, which include most dielectrics. Quadrant II are materials such as metals that exhibit a negative permittivity below the plasma frequency. Quadrant IV are materials with a negative permeability, such as Ni-Zn ferrite. Materials in quadrant III have simultaneous negative permittivity and permeability, a property that is not found in natural materials. Examples of metamaterials are engineered materials having a negative permittivity, negative permeability, and/or negative refractive index within a frequency band.

There are several proposed designs for metamaterials. The fishnet, omega, and S-shaped metamaterials have been experimentally shown to exhibit a negative index [22-24]. The wire and concentric SRR structures are studied in the simulations and presented later in this section. A single ring SRR structure was studied in this project, both in simulations and measurements (see below).

There have been several proposed methods for characterizing the effective constitutive parameters of composite materials such as wire and split-ring resonator arrays, with a purpose of demonstrating the existence of an effective negative permittivity and permeability over some frequency band. For example, in [19, 26-29], the plane wave normal incidence approach was discussed for retrieving the effective parameters; [30] presented an optimization technique; and in [31] a waveguide approach for retrieving the anisotropic parameters was presented. With the exception of [30], these methods involve retrieving the effective parameters from the measured or simulated scattering parameters. In this project, the retrieval method for a homogeneous, isotropic medium and the analysis of the waveguide retrieval method for a homogeneous, anisotropic medium are presented in detail.

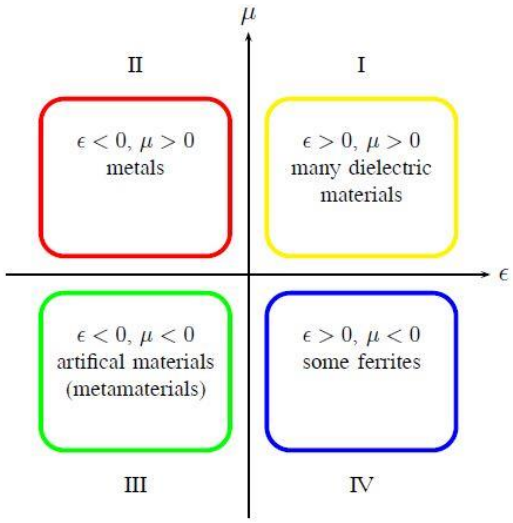

Figure 4: All materials can be mapped into one of the four quadrants described by their electric permittivity and magnetic permeability.

A split-ring resonator structure was later shown by Pendry *et al.* [25] to exhibit a negative real permeability over a frequency bandwidth. This structure was used in many interesting designs and applications, including negative index materials [19, 27, 32, 33], electromagnetic cloaks [1, 4], and filters [34]. SRRs have also been shown to exhibit negative permittivity [35, 36]. We investigated this property is further investigated with HTS SRRs. Many of the demonstrated circuits exhibit significant loss, which can be reduced by using superconductors. Ricci *et al.* [37-39] investigated superconducting metamaterials made of Niobium (Nb) SRRs deposited on single crystal quartz substrates and Nb wires. Nb has a critical temperature T_c of ≈ 9.2K and requires, e.g., the use of liquid Helium for cooling. Chen *et al.* [40] studied the resonant properties of terahertz HTS Jerusalem cross metamaterial, made of $YBa_2Cu_3O_{7-\delta}$ (YBCO) with δ=0.05 and has a T_c of 90K. The use of HTS in metamaterial designs is of interest since experiments can be carried out with liquid nitrogen or low cost, low power cryocoolers.

To demonstrate the negative permeability, we modeled a plane wave incident on an array of SRRs in HFSS, with the magnetic field component normal to the plane of the split-ring resonator, as shown in Figure 5. Electric and magnetic walls mirror the SRR into an infinite array. As with the wire effective medium, the SRR is assumed to make up an effective homogeneous, isotropic medium of thickness L in the propagating direction. The extracted relative permeability, Figure 5b, shows a negative real part between 9.97GHz and 11.69GHz. The figure also shows a near-zero relative permeability at frequencies above 11.69GHz. This is of particular interest because the values of μ_r required for the metamaterial radome range from 0 to 0.5 for the example in Figure 4.

A composite material that combines the SRR and wire arrays can simultaneously have effective negative permeability, negative permittivity, and negative refraction index in a frequency band. To demonstrate this, a SRR-wire unit cell was modeled in HFSS, as shown in Figure 5a, which also includes the polarization of the incident plane wave. Again, the electric and magnetic walls mirror the unit cell into an infinite array. By assuming a homogeneous, isotropic medium for this structure, the effective relative permeability and permittivity are obtained from the S-parameters. The negative permeability and

permittivity are still present, seen in Figure 5b and 5c. In addition, Figure 5d also shows a frequency bandwidth with a negative refractive index n'. A similar structure had been constructed and tested by Shelby *et al.* [32]. In his experiment, a wave with an 18° incident angle at the metamaterial/air boundary refracts at -61°, corresponding to a refractive index of -2.7 at 10.5GHz.

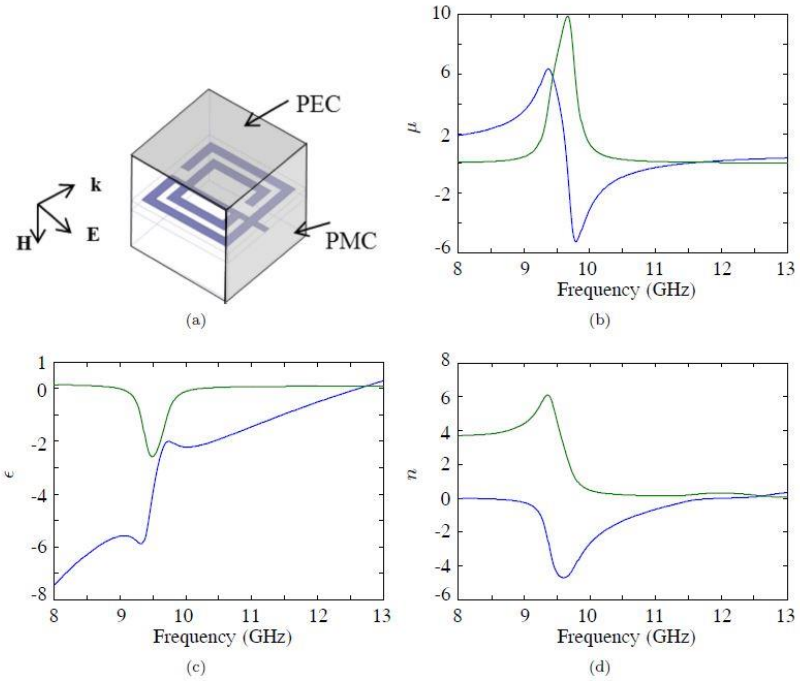

Figure 5: (a) The unit cell of the SRR metamaterial has dimensions of 2.5mm$\times$2.5mm$\times$2.5mm, with the outer SRR width = 2.2mm, line width = 0.2mm, gap = 0.3mm, and separation between the two rings = 0.15mm. (b) The extracted effective relative permeability where the blue and green curves represent μ' and μ'', respectively. (c) and (d) show the effective relative permittivity and refractive index, respectively. The blue and green curves represent the ' and '' values.

Constitutive Parameter Transformations

Above we discussed an electromagnetic guiding structure (metamaterial cloak), which has material properties that depend on its geometry and dimensions. In order to guide the EM wave around a cylindrical cloak, thus fully isolating the interior and not disturbing the exterior field pattern, the structure must ideally have the following permeability and permittivity properties:

$$\frac{\boldsymbol{\mu}}{\mu_0} = \frac{\boldsymbol{\epsilon}}{\epsilon_0} = \text{diag}\left[\frac{r-a}{r},\ \frac{r}{r-a},\ \left(\frac{b}{b-a}\right)^2 \frac{r-a}{r}\right] \quad \text{(Cylindrical)}$$

Transformation mathematics is used here for deriving the material properties of an EM guiding structure. Details are described in the thesis of Frank Trang in Chapter 2 and Appendix A. The relative permittivity and permeability tensors for a cylindrical radome of inner radius a and outer radius b are obtained. It can be seen that all the quantities are spatially varying and the ϕ components are infinite at

r=a. Thus, designing a material with these properties is difficult, if not impossible. Because the radome is measured inside a parallel plate waveguide, the only relevant parameters are μ_r, μ_ϕ, and ε_z.

Resonant Response of HTS SRR

Each HTS SRR is made up of two 700nm thick YBCO rings deposited on top of a 500μm thick, $1cm^2$ MgO substrate that has a nominal relative permittivity of 9.7. Figure 6 shows a photograph of a SRR element, with relevant dimensions. A 100nm coating of CeO_2 is applied over the YBCO SRRs. A single photoresist contact mask was used in the photolithography process of patterning the SRRs.

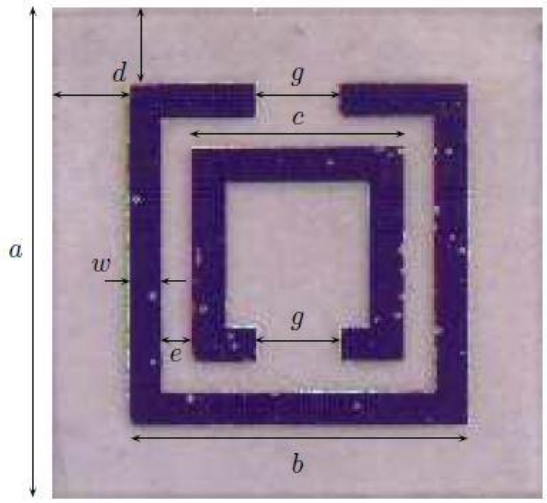

Figure 6: A close-up photograph of the SRR unit cell with labeled dimensions, where a=10mm, b=7mm, c=4.4mm, d=1.5mm, e=0.5mm, g=1.6mm, w=0.8mm.

The waveguide environment was chosen for measurements because the waveguide components can easily be confined into a cryogenic enclosure and thus can easily be temperature controlled and calibrated. A vacuum sealed cylindrical cryostat is used to confine and cool the waveguide components, which include two aluminum waveguide to coaxial adapters and a 76.2mm copper waveguide section for holding the HTS SRRs, as shown in Figure 7. The inner diameter of the cryostat is 74mm and wide enough to hold the waveguide components.

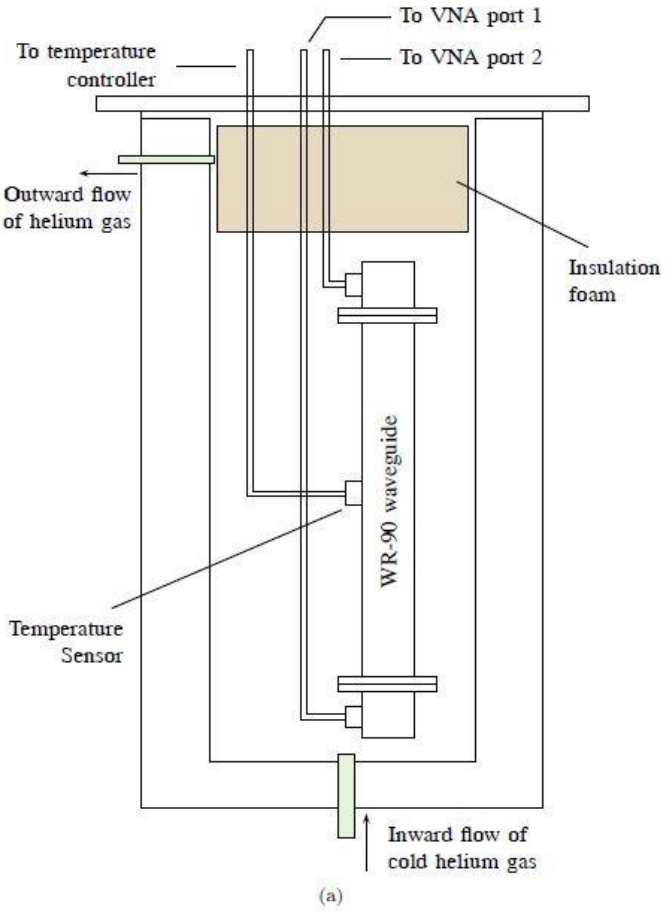

Figure 7: (a) A sketch of the cryostat with waveguide components. (b) A photograph of the waveguide setup that fits inside the cryostat.

Two feed-throughs in the top metal lid allow the rigid copper coaxial cables to connect to a vector network analyzer (VNA). The temperature of the copper waveguide is monitored with an attached temperature sensor. Figure 7a is a sketch that shows the placement of the various components inside the cryostat along with the gas flow directions. In the measurement presented here, a variable temperature cryostat is used to investigate a wider range of temperature. Although liquid nitrogen would suffice in cooling our structure to sub-T_C temperature, we were also interested in the responses

at temperatures down to 40K. Figure 7b shows a photograph of the waveguide unit that is placed in the flow-type cryostat, where the cold helium gas is supplied from a liquid helium dewar. The temperature of the waveguide components is regulated by a LakeShore 330 autotuning temperature controller and TRW flow control unit. With this setup, we studied the HTS SRRs from room temperature to 40K.

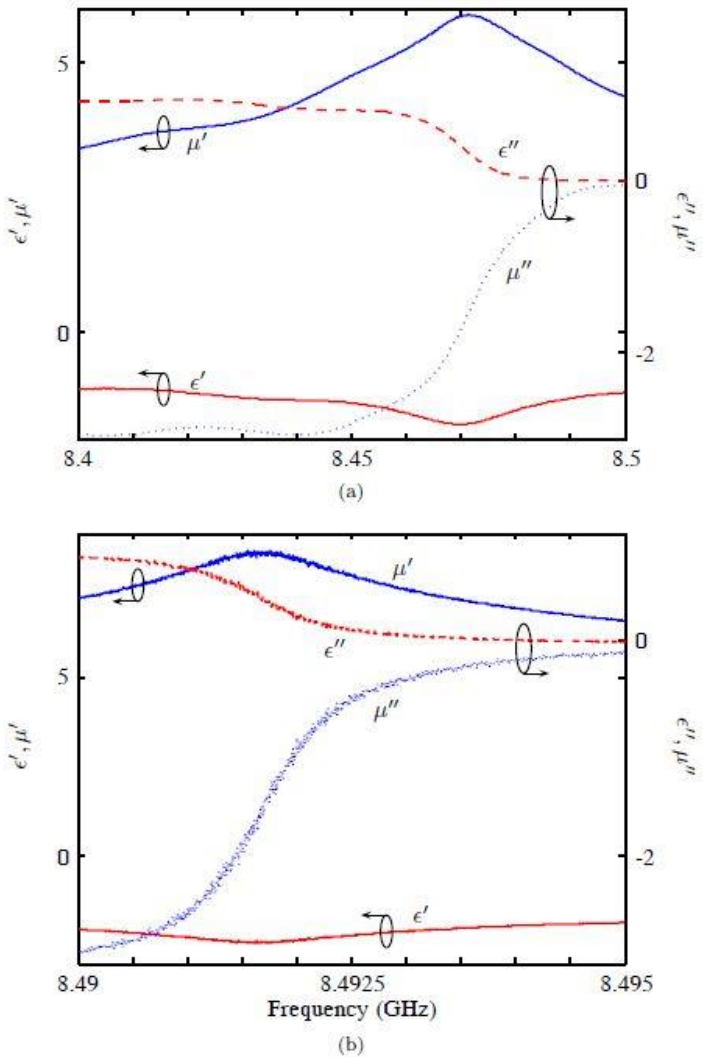

Figure 8: The extracted relative permittivity and permeability at (a) 89K and (b) 88K.

An array of seven YBCO on MgO split ring resonators was simulated and measured inside a WR-90 waveguide showing a pronounced wide stop band centered around 8GHz. Furthermore, a single element ring was measured for studying the resonant frequency and quality factor versus temperature. By fitting the behavior of the resonant frequency to an expression that relates it to the London penetration depth, kinetic inductance, and critical temperature, we can infer their values. The fitted T_c of 91.3K and f_r of 8.53GHz are close to the observed values. The inferred magnetic penetration depth $\lambda(0)$ of 395nm is higher than typical literature values, but still within an acceptable range. This can be attributed to the slight damaging of the YBCO film due to overexposure during the photolithography

process. The kinetic inductance was shown to saturate at low temperature and vary greatly close to the T_c. The quality factor, saturating at >5000, of these HTS SRRs was shown to be much higher than the normal conductor samples. A peak of Q≈42000 was observed around 87K. Finally, we have shown that these HTS SRRs have electric resonances and exhibit a negative effective permittivity in the neighborhood of the resonance.

Effective Constitutive Parameters of HTS SRR

Arrays of the HTS SRRs were placed inside an X-band rectangular waveguide, with orientations I and II shown in Figures 9(a) and 9(b), respectively. For orientation I, nine evenly spaced 4x1 SRR strips were axially inserted into the waveguide, totaling 36 SRRs. A single 4x9 sample was used for the transverse orientation II, again with 36 SRRs. Note that the conducting SRRs are alternately flipped in the vertical direction. This is done so that when image theory is applied along the waveguide walls, the arrays look infinitely periodic in the x and y directions. Also, as pointed out by Smith *et al.*[64], the symmetrical arrangement of the SRRs, as in our case, reduces the magneto-electric coupling that is responsible for the bi-anisotropic behavior. For both cases, the dominant TE_{10} mode is excited in the waveguide, which has the electric field in the y direction (Figures 9(c) and 9(d)), or along material axis 2.

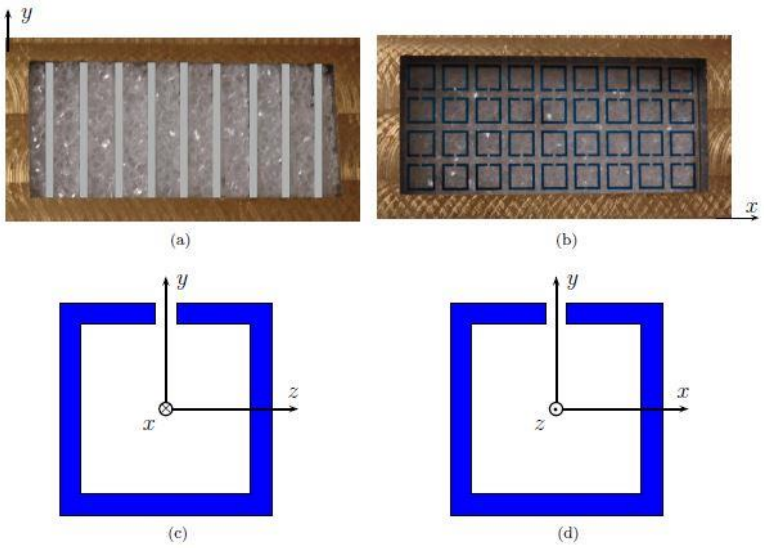

Figure 9: Photographs of diced 4x1 and 4x9 YBCO SRR arrays on MgO substrate aligned inside a WR-90 waveguide with orientations (a) I and (b) II, respectively, for measurements. The gray bars in (a) are included to clearly mark the locations of the 4x1 strips. The material axes corresponding to the Cartesian axes are shown for orientations (c) I and (d) II.

For each of the two measurements, the S parameters were de-embedded to the material reference planes, and the transmission and reflection coefficient magnitudes are shown in Figure 10. The stop band about 9.5GHz in Figure 10a suggests a region of negative μ_1 and positive ε_2. Measurements of the 4x9 array, Figure 10b, show eight high-Q resonances in addition to the main resonance at ≈9.7GHz. Using the S parameters from these two measurements, the three parameters, μ_1, ε_2, and μ_3 are calculated from the formulae discussed earlier, with the results shown in Figure 11.

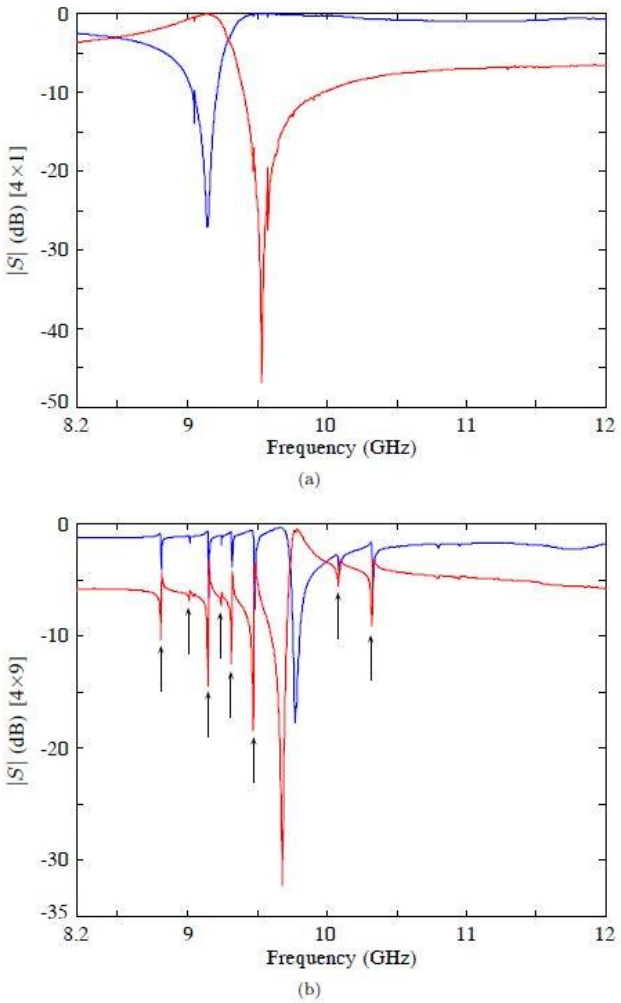

Figure 10: Measured reflection (S_{11}, blue curve) and transmission (S_{21}, red curve) coefficient magnitudes of (a) the nine 4x1 SRR strips and (b) 4x9 SRR array, respectively, placed inside the waveguide section with the whole structure cooled to ≈76K. The markers in (b) indicate the locations of the sharp resonances.

The magnetic plasma frequency of this resonant structure is 10.45GHz, $\mu_1'=0$ in Figure 11a. Just below this frequency, between 9.25GHz and 10.45GHz, the real part of the relative permeability μ_1' is negative, which is consistent with previously published work on SRRs. Generally, the imaginary part μ_1'', corresponding to loss, is large in this frequency band for room temperature normal conducting SRRs. The extracted value from the HTS SRR arrays however shows that at frequencies above the frequency where μ_1' is at its minimum, μ_1'' quickly drops to near-zero. This is a property that is not observed in normal conducting SRRs on lossy substrate, as shown in the extracted μ_1 for the copper SRRs on a Rogers 3010 substrate. The Rogers 3010 substrate has a dielectric constant of 10.2 with an loss tangent of 0.0022 at 10GHz. The magnetic loss tangents ($\tan \delta_\mu = |\mu''/\mu'|$) for the Cu SRR array at $f(\mu'_{min})$=9.59GHz and $f(\mu'_{min})$+100MHz are 0.911 and 0.523, respectively, a 42\% reduction. The $\tan \delta_\mu$ for the HTS SRR array at $f(\mu'_{min})$=9.53GHz and $f(\mu'_{min})$+100MHz are 0.324 and 0.068, respectively, a 79\% reduction. In Figure 11c, we notice that ε'' is negative at frequencies just above where ε' is at a minimum. This is also seen in many published works on SRRs.

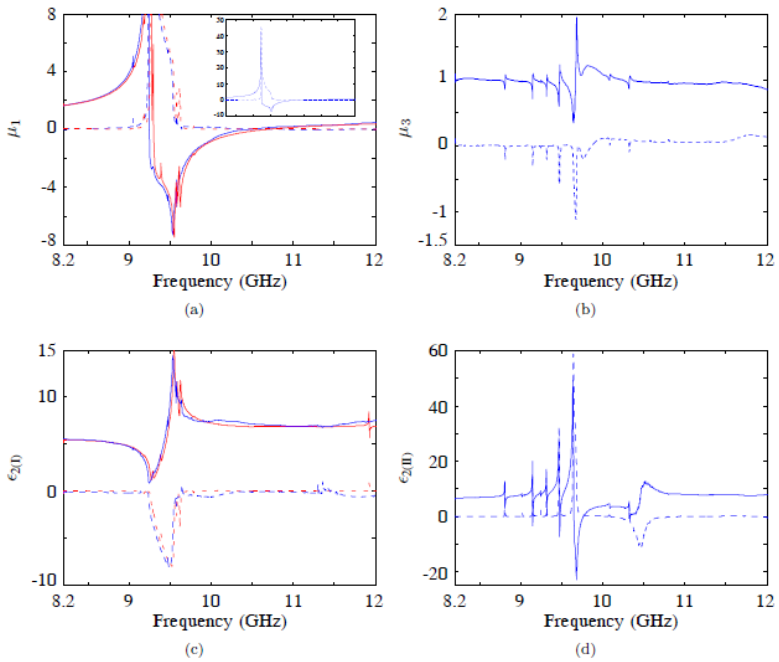

Figure 11: {Effective parameters extracted from waveguide measurements of the two oriented samples, with (a) zoomed in μ_1, (b) μ_3, (c) $\varepsilon_{2(I)}$, and (d) $\varepsilon_{2(II)}$. The blue and red curves are measurements and waveguide simulations, respectively. The solid and dashed curves represent the real (') and imaginary (") parts, respectively. The inset plot in (a) shows the full μ_1 from the measurement.

Radome Measurement

The measurement setup was chosen to be a parallel plate waveguide (PPW) that has the 10mm height of the cylindrical radome. A sketch of the cross section cut of the waveguide is shown in Figure 12. The waveguide is constructed of two single-sided copper cladding FR-4 substrates. Emerson and Cuming LS-24 non-magnetic absorber wedges were placed at the edges to reduce reflection from the finite extend of the waveguide. The absorbers also help to maintain a 10mm separation between the FR-4 sheets. Two 50Ω coaxial probes were used; one acts as a transmitter to excite an EM wave inside the waveguide and one as a receiver. Each probe has a 0.28mm diameter center conductor extending 6mm into the waveguide.

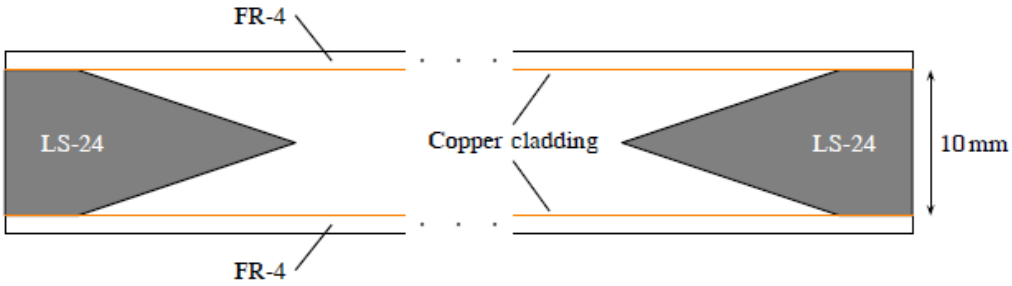

Figure 12: Cross section sketch of the parallel plate waveguide for characterizing the metamaterial radome. The FR-4 copper cladding thickness is 35µm, respectively. LS-24 absorber wedges were placed along the boundaries of the parallel plate waveguide to minimize reflection and provide a constant spacing between the two plates.

A three layer Cu-radome was studied in the 300x240mm^2 PPW, in both the simulations and measurements. The radii of the inner layer (layer 1), middle layer (2) and outer layer (3) are 12.226mm, 14.688mm and 17.147mm, respectively, shown in Figure 13. Layers 1, 2, and 3 have 30, 36, and 42 of the 4x1 SRR strips, respectively, with every strip having the same SRR dimensions. The measured and simulated S_{21} are shown in Figure 14. We clearly see agreement between the measurements and simulations. Note that the SRR dimensions have not been optimized for isolation and shadowing. Although the respective S_{21} curves are shifted in frequency, the features in both the simulation and measurement results are the same. In the simulations, the isolation and shadowing at 10.9GHz are 5.3dB and 3.4dB, respectively. In the measurements, they are 6.1dB and 3.9dB, respectively, at 11.35GHz.

Figure 13: Three layer radome with uniform SRR dimensions in all the layers.

The parallel plate waveguide setup was also used for measuring the radome constructed of YBCO SRR arrays. The measurement environment needs to be cooled down to below the T_C of YBCO (≈88K). For the PPW to be cooled and thermally insulated from the warmer surrounding, it is enclosed inside a stainless steel box, in which the interior is cooled by a SunPower CryoTel GT cryocooler and liquid nitrogen.

Figure 15 shows the cross-section sketch of the cryogenic setup along with dimensions of the various pieces. The stainless steel box provides structural stability and helps maintain the internal temperature. At the base of the box is an orifice of 47.625mm diameter to which a NW50 flange is welded. This allows the cryocooler to be tightly attached with only the cold tip protruding into the box. As the name suggests, the cold tip is the part that gets cooled to cryogenic temperature. A 70x70mm^2 of thickness 6mm block of copper fits firmly on the cold tip. A Lakeshore temperature sensor is attached to the copper block, with the temperature being fed back to the cryocooler controller for power regulation. Not shown in the figure is a fan that cools the cryocooler.

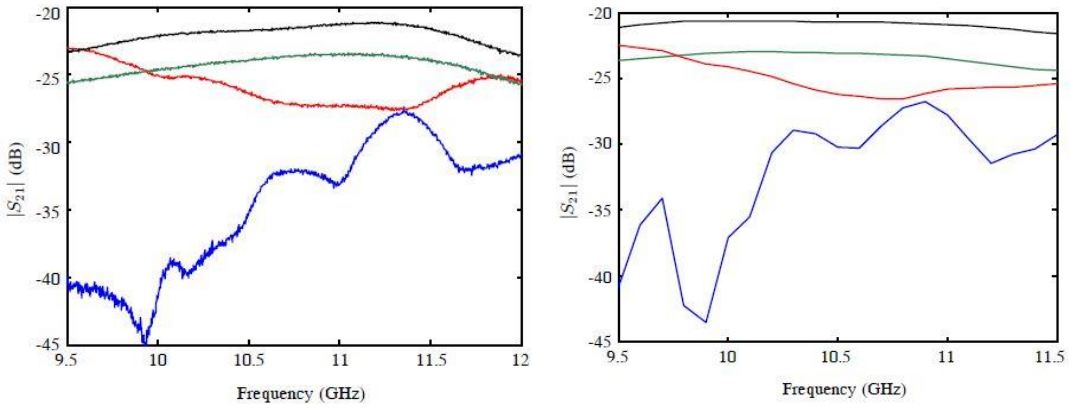

Figure 14: (left) Measured transmission coefficient with the receiver probe placed at the center (red curve) and 70mm behind the three layer radome (blue curve) from Figure 13. The black and green curves are the respective measurements of an empty 300x240mm^2 PPW.
(right) Simulated transmission coefficient with the receiver probe placed at the center (red curve) and 70mm behind the three layer radome (blue curve). The black and green curves are the respective simulation of an empty 300x240mm^2 PPW.

The PPW is again formed by two single sided copper cladding FR4. Two copper plates could have been used instead. However, the heat conduction of the copper would prevent a localization of the cold temperature at the center of the PPW, where the HTS radome resides. A 70x70mm^2 hole is cut at the center of the bottom FR-4 sheet, to allow the copper block to fit tightly flushed into the hole. Copper tape is lined along the sides of the square hole to ensure electrical conductivity between the copper cladding and the copper block. Thus, the holed FR-4 board together with the square copper block form a contiguous conducting plate. A thick block of Rohacell IG-71 foam is placed underneath the FR-4 sheet for structural support and used also as a thermal insulator to the base of the steel box. At low temperature, the thin sheet of FR-4 does not remain flat. Therefore it is securely adhered to the supporting foam. 10mm height LS-24 absorbers separate the two sheets of FR-4 to form the parallel plate waveguide.

The absorber helps reduce the reflection from the finite size PPW and also maintain a constant distance between the top and bottom FR-4 sheet. Another thick Rohacell foam block on the top maintains the flatness of the top FR-4 sheet and doubles as a thermal insulator. Three holes were drilled on the steel lid, top layer foam, and FR-4 sheet for the coaxial probes to be inserted into the parallel plate waveguide. The probes are connected to a VNA for measuring the transmission coefficients.

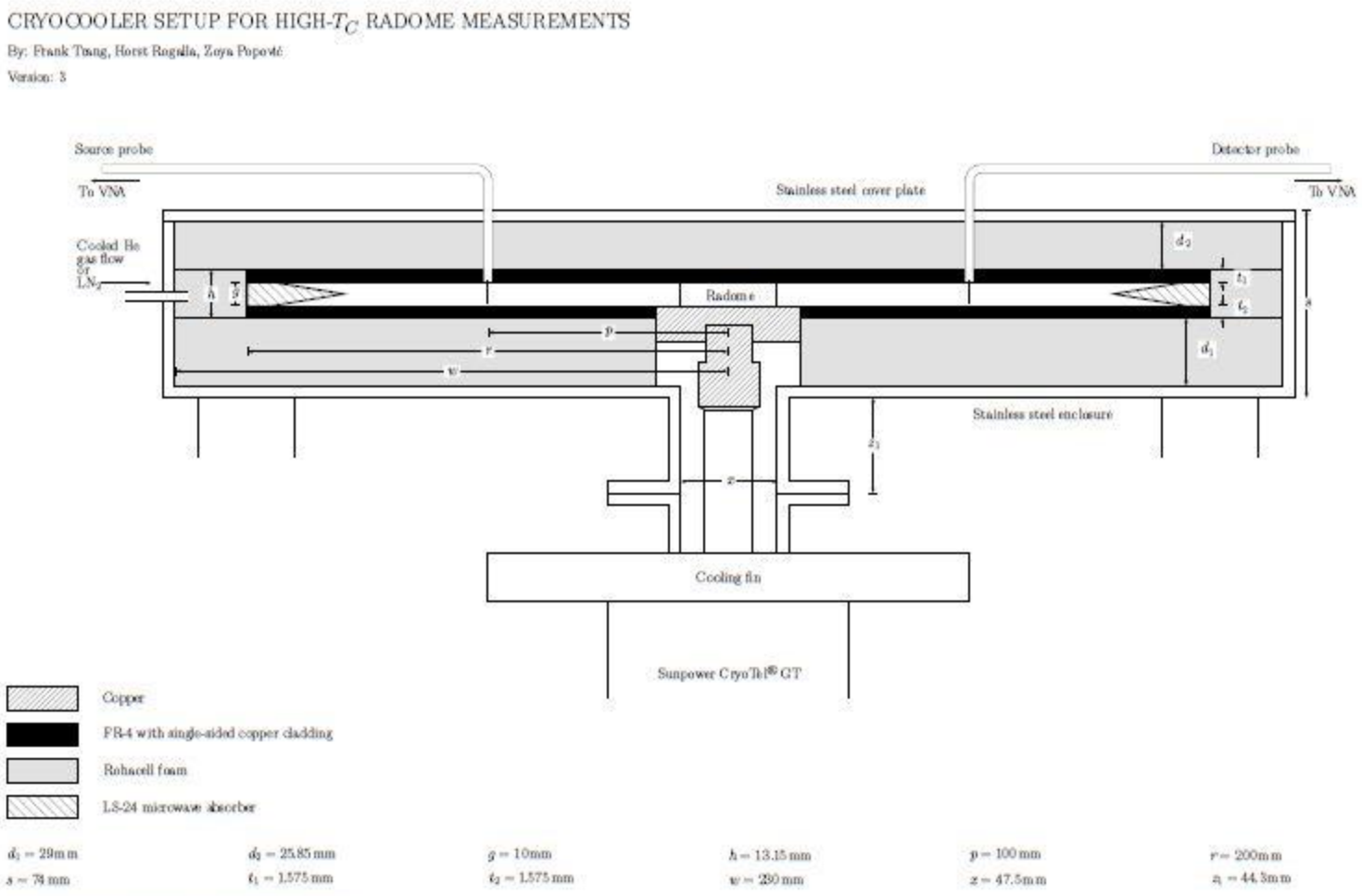

Figure 15: Cross section sketch of the cryogenic measurement setup. The parallel plate is enclosed inside a steel box and is cooled by a SunPower Cryotel GT cryocooler from the base of the box.

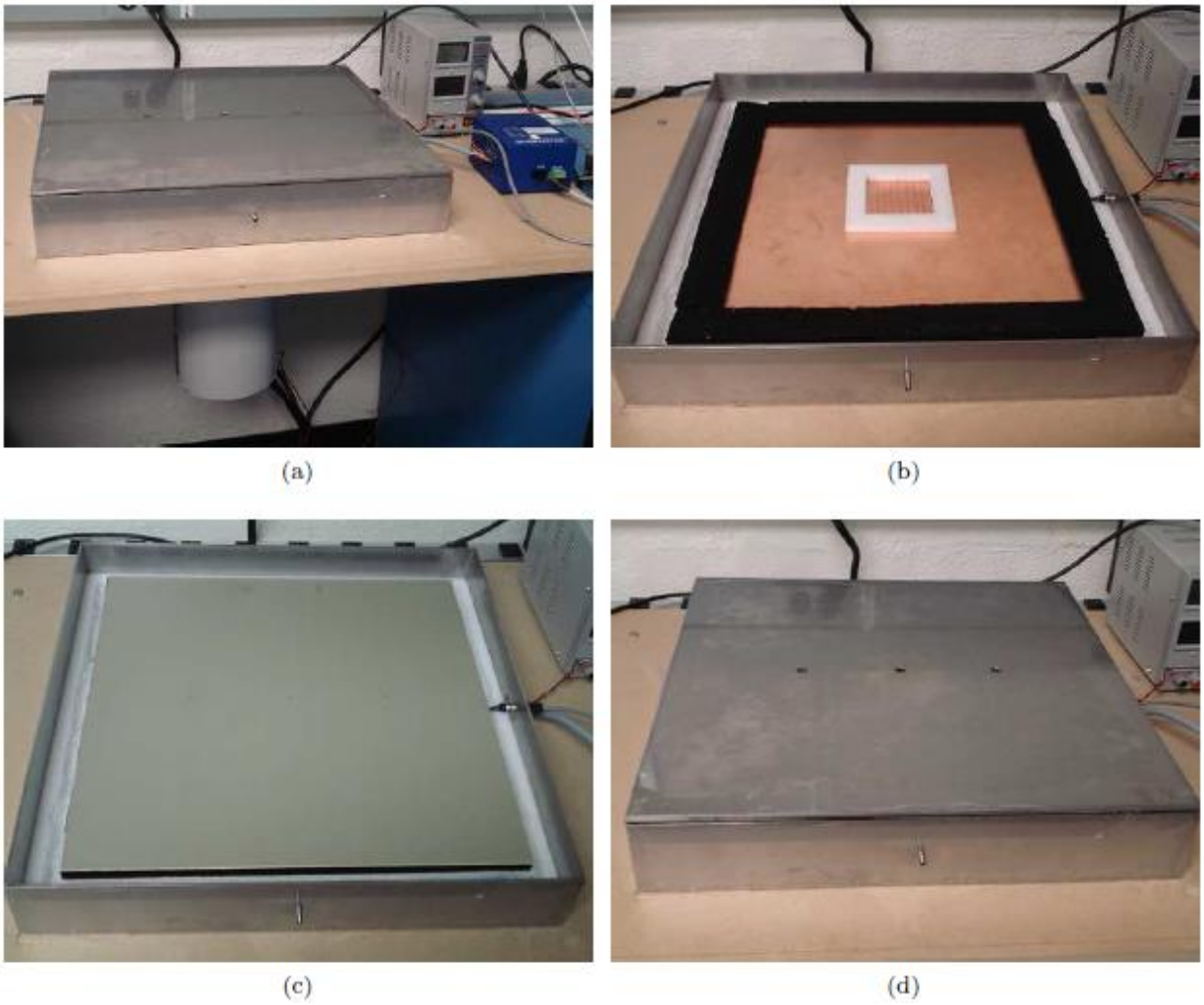

Figure 16: Cryogenic setup photographs of (a) the full setup, (b) the setup without the top FR-4 sheet, (c) the setup with the full PPW, and (d) the setup with the enclosing stainless steel lid.

The final measurement setup is shown in Figure 16. For structural stability, the steel box sits firmly on a 1 inch thick slab of wood, which is bolted on two steel rails. The rail is bolted to the two cabinets. It turned out that the cryocooler in the current setup could not cool the radome to sub-T_C of YBCO. This is mainly due to the poor thermal insulation in the setup. Therefore, grooves were cut into the foam around the PPW and filled with liquid nitrogen to reduce the heat load to the cryocooler. This helped brought the whole setup to 77K.

The fabricated three-layer YBCO SRR radome was measured in the cryogenic setup environment. The SRR dimensions result from the optimization. The inner, middle, and outer layers have 30, 36, and 42 SRR array elements, each 2.5x10mm^2 and consists of four 700nm thick YBCO SRRs on a 500µm thick MgO substrate. Figure 17 shows a photograph of the HTS radome.

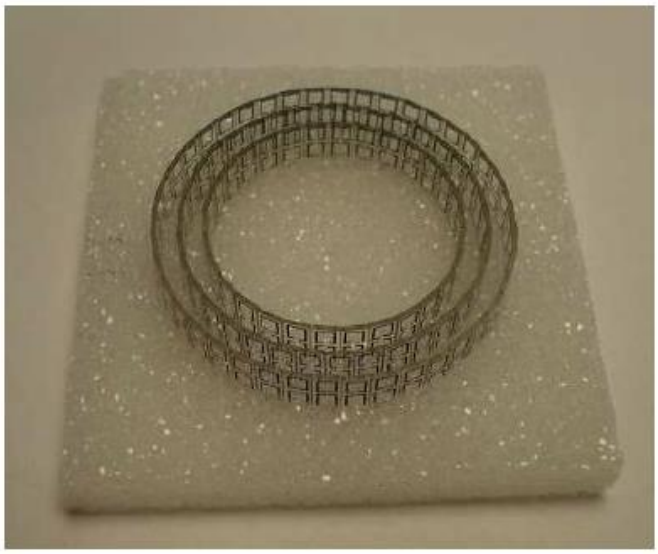

Figure 17: The fabricated three layer YBCO SRR on MgO radome with the optimized SRR dimensions.

A series of isolation and shadowing measurements were taken at sub-T_C temperatures. The optimal frequency of isolation may shift due to the temperature variation. The optimal frequency in the neighborhood of 11GHz for reduction stays constant at ≈11.12GHz. From these measurements, the optimal set is shown in Figure 18.

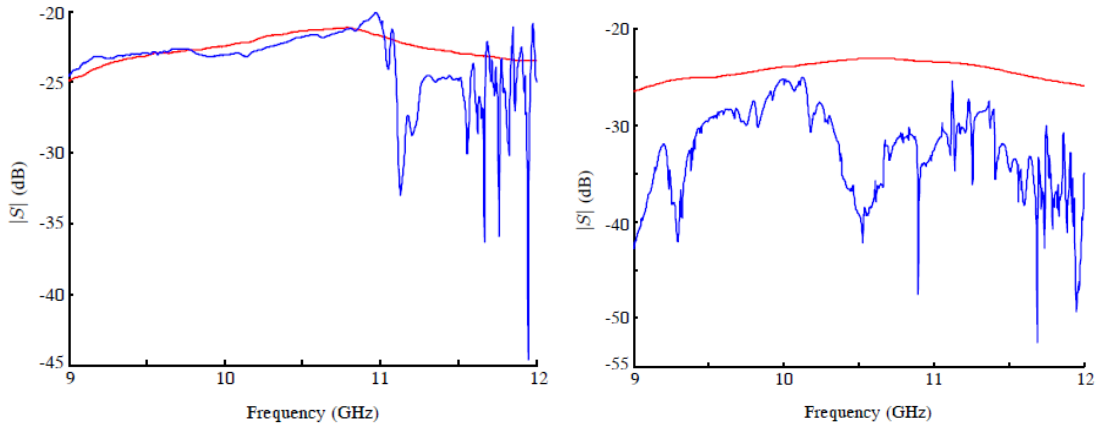

Figure 18: (left) Cold temperature measurements of the YBCO SRR radome for isolation (receiver probe placed at the radome center). The dashed red curve shows the empty PPW measurement.
(right) Cold temperature measurements of the YBCO SRR radome for shadowing (receiver probe placed 100mm behind the radome). The dashed red curve shows the empty PPW measurement.

The zoomed-in plots for the optimal set are shown in Figure 19. At 11.12GHz, the isolation is ≈10.5dB and the shadowing is ≈1.9dB. The measurements show better isolation than both the copper and YBCO SRR radomes in the simulations. The measured shadowing is lower than the simulated YBCO SRR radome, but greater than the simulated copper SRR radome. The results in suggests that the frequency band for low shadowing is very restrictive, whereas the frequency band for high isolation is tunable. Thus, one would want to operate at the frequency with the lowest shadowing, provided that we are still

in the isolation bandwidth. This work demonstrates the feasibility of fabricating a structure that provides good isolation between two antennas and low disturbance of the transmitted fields.

References

[1] S. A. Cummer, B.-I. Popa, D. Schurig, D. R. Smith, and J. Pendry, "Full-wave simulations of electromagnetic cloaking structures," *Physical Review E*, vol. 74, p. 036621, Sep. 2006. 2, 5, 7, 11, 29

[2] J. B. Pendry, D. Schurig, and D. R. Smith, "Controlling electromagnetic fields," *Science*, vol. 312, no. 5781, pp. 1780–1782, 2006. 2, 5

[3] B. Kanté, A. de Lustrac, J.-M. Lourtioz, and S. N. Burokur, "Infrared cloaking based on the electric response of split ring resonators," *Opt. Express*, vol. 16, pp. 9191–9198, Jun 2008. 2, 5

[4] D. Schurig, J. J. Mock, B. J. Justice, S. A. Cummer, J. B. Pendry, A. F. Starr, and D. R. Smith, "Metamaterial electromagnetic cloak at microwave frequencies," *Science*, vol. 314, pp. 977–980, 2006. 2, 5, 7, 11, 29, 44, 65, 70, 89

[5] B. Kanté, D. Germain, and A. de Lustrac, "Experimental demonstration of a nonmagnetic metamaterial cloak at microwave frequencies," *Phys. Rev. B*, vol. 80, p. 201104, Nov 2009. 2, 44, 65, 89

[6] G. Breed, "Basic principles of electrically small antennas," *High Frequency Electronics*, vol. 6, p. 50, February 2007. 4

[7] C. A. Balanis, *Antenna Theory: Analysis and Design*. John Wley & Sons, 3 ed., 2005. 4

[8] W. G. Lyons, D. R. Arsenault, A. C. Anderson, T. G. Sollner, P. G. Murphy, M. M. Seaver, R. R. Boisvert, R. L. Slattery, , and R. W. Ralson, "High-*tc* superconductive wideband compressive receivers," *The Lincoln Laboratory Journal*, vol. 9, no. 1, p. 33, 1996. 4

[9] H. Chaloupka, N. Klein, M. Peiniger, H. Piel, A. Pischke, and G. Splitt, "Miniaturized high-temperature superconductor microstrip patch antenna," *Microwave Theory and Techniques, IEEE Transactions on*, vol. 39, pp. 1513 –1521, sep 1991. 4

[10] G. B. Walker and C. R. Haden, "Superconducting antennas," *Journal of Applied Physics*, vol. 40, no. 5, pp. 2035–2039, 1969. 4

[11] J. James, M. White, D. Steel, J. Carney, and M. Gledhill, "System considerations of a superconducting loop antenna," in *Electrically Small Antennas, IEE Colloquium on*, pp. 7/1–7/4, 1990. 4

[12] J. G. Bednorz and K. A. Müller, "Possible high *Tc* superconductivity in the Ba-La-Cu-O system," *Zeitschrift für Physik B Condensed Matter*, vol. 64, pp. 189–193, 1986. 10.1007/BF01303701. 4

[13] M. K. Wu, J. R. Ashburn, C. J. Torng, P. H. Hor, R. L. Meng, L. Gao, Z. J. Huang, Y. Q. Wang, and C. W. Chu, "Superconductivity at 93 K in a new mixed-phase Y-Ba-Cu-O compound system at ambient pressure," *Physical Review Letters*, vol. 58, pp. 908–910, Mar. 1987. 4

[14] “Sunpower inc..” http://www.sunpowerinc.com. 4

[15] A. J. Ward and J. B. Pendry, “Refraction and geometry in maxwell’s equations,” *Journal of Modern Optics*, vol. 43, no. 4, pp. 773–793, 1996. 5, 17, 125

[16] D. Schurig, J. B. Pendry, and D. R. Smith, “Calculation of material properties and ray tracing in transformation media,” *Opt. Express*, vol. 14, pp. 9794–9804, Oct 2006. 5, 17

[17] P. Zhang, *Theory of transformation optics and invisibility cloak design*. PhD thesis, KTH Royal Institute of Technology, 2011. 5, 17, 99, 125

[18] S. A. Ramakrishna and T. M. Grzegorczyk, *Physics and Applications of Negative Refractive Index Materials*. CRC Press, 1st ed., 2008. 8

[19] D. R. Smith, D. C. Vier, T. Koschny, and C. M. Soukoulis, “Electromagnetic parameter retrieval from inhomogeneous metamaterials,” *Physical Review E*, vol. 71, p. 036617, Mar. 2005. 8, 11, 29, 43

[20] J. B. Pendry, A. J. Holden, W. J. Stewart, and I. Youngs, “Extremely low frequency plasmons in metallic mesostructures,” *Phys. Rev. Lett.*, vol. 76, pp. 4773–4776, Jun 1996. 8, 9, 10

[21] T. Tsutaoka, T. Nakamura, and K. Hatakeyama, “Magnetic field effect on the complex permeability spectra in a niâASzn ferrite,” *Journal of Applied Physics*, vol. 82, no. 6, 1997. 8

[22] C. Sabah and H. G. Roskos, “Numerical and experimental investigation of fishnet-based metamaterial in a x-band waveguide,” *Journal of Physics D: Applied Physics*, vol. 44, no. 25, p. 255101, 2011. 8, 9

[23] E. Lheurette, G. Houzet, J. Carbonell, F. Zhang, O. Vanbesien, and D. Lippens, “Omega-type balanced composite negative refractive index materials,” *Antennas and Propagation, IEEE Transactions on*, vol. 56, no. 11, pp. 3462–3469, 2008. 8, 9

[24] H. Chen, L. Ran, J. Huangfu, X. Zhang, K. Chen, T. M. Grzegorczyk, and J. Au Kong, “Left-handed materials composed of only s-shaped resonators,” *Phys. Rev. E*, vol. 70, p. 057605, Nov 2004. 8, 9

[25] J. Pendry, A. Holden, D. Robbins, and W. Stewart, “Magnetism from conductors and enhanced nonlinear phenomena,” *IEEE Trans. Micr. Theory Tech.*, vol. 47, pp. 2075 –2084, 1999. 9, 10, 29

[26] U. Hasar and J. Barroso, “Permeability measurement of metamaterials with split-ring-resonators using free-space calibration-independent methods,” *J. Infrared, Millimeter, and Terahertz Waves*, vol. 33, no. 2, pp. 218–227, 2012. 8, 43

[27] X. Chen, T. M. Grzegorczyk, B.-I. Wu, J. Pacheco, and J. A. Kong, “Robust method to retrieve the constitutive effective parameters of metamaterials,” *Physical Review E*, vol. 70, p. 016608, Jul. 2004. 8, 11, 29, 43

[28] D. R. Smith, S. Schultz, P. Markoš, and C. M. Soukoulis, "Determination of effective permittivity and permeability of metamaterials from reflection and transmission coefficients," *Phys. Rev. B*, vol. 65, p. 195104, Apr 2002. 8, 43

[29] Z. Szabo, G.-H. Park, R. Hedge, and E.-P. Li, "A unique extraction of metamaterial parameters based on kramers-kronig relationship," *IEEE Trans. Micr. Theory Tech.*, vol. 58, no. 10, pp. 2646–2653, 2010. 8, 43

[30] X. Chen, T. M. Grzegorczyk, and J. A. Kong, "Optimization approach to the retrieval of the constitutive parameters of slab of general bianisotropic medium," *Prog. in Electr. Res.*, vol. 60, pp. 1–18, 2006. 8, 43

[31] H. Chen, J. Zhang, Y. Bai, Y. Luo, L. Ran, Q. Jiang, and J. A. Kong, "Experimental retrieval of the effective parameters of metamaterials based on a waveguide method," *Opt. Express*, vol. 14, pp. 12944–12949, Dec 2006. 8, 43, 45

[32] R. A. Shelby, D. R. Smith, and S. Schultz, "Experimental verification of a negative index of refraction," *Science*, vol. 292, pp. 77–79, 2001. 11, 12, 29, 44

[33] L. Ran, J. Huangfu, H. Chen, X. Zhang, K. Cheng, T. M. Grzegorczyk, and J. A. Kong, "Experimental study on several left-handed metamaterials," *Progress in Electromagnetics Research*, vol. 51, pp. 249–279, 2005. 11, 29

[34] M. Gil, J. Bonache, and F. Martín, "Metamaterial filters: A review," *Metamaterials*, vol. 2, no. 4, pp. 186– 197, 2008. 11, 29

[35] S. Linden, C. Enkrich, M. Wegener, J. Zhou, T. Koschny, and C. M. Soukoulis, "Magnetic response of metamaterials at 100 terahertz," *Science*, vol. 306, no. 5700, pp. 1351–1353, 2004. 11, 31, 40

[36] T. Koschny, M. Kafesaki, E. N. Economou, and C. M. Soukoulis, "Effective medium theory of left-handed materials," *Physical Review Letters*, vol. 93, p. 107402, Sep. 2004. 11, 31, 40

[37] M. Ricci, N. Orloff, and S. M. Anlage, "Superconducting metamaterials," *Applied Physics Letters*, vol. 87, no. 3, p. 034102, 2005. 11, 44

[38] M. C. Ricci and S. M. Anlage, "Single superconducting split-ring resonator electrodynamics," *Applied Physics Letters*, vol. 88, no. 26, p. 264102, 2006. 11, 44

[39] M. Ricci, H. Xu, R. Prozorov, A. Zhuravel, A. Ustinov, and S. Anlage, "Tunability of superconducting metamaterials," *IEEE Transactions on Applied Superconductivity*, vol. 17, pp. 918 –921, Jun. 2007. 11,44

Publications

1 F. Trang, H. Rogalla, and Z. Popović, "Effective Constitutive Parameters of High-Temperature Superconducting Split-Ring Resonator Arrays",
IEEE Transactions on Applied Superconductivity, to be published.

2 F. Trang, "Cryogenic Microwave Anisotropic Artificial Materials", Thesis,
University of Colorado at Boulder, Department of Electrical, Computer, and Energy Engineering (2013)

3 F. Trang, H. Rogalla, and Z. Popović, "Resonant Response of High-Temperature Superconducting Split-Ring Resonators",
IEEE Transactions on Applied Superconductivity 23, 1300405 (2013).

4 F. Trang, E. F. Kuester, H. Rogalla, and Z. Popović, "Sensitivity of Double-Sided Split Ring Resonator Arrays to Fabrication Tolerances",
arXiv e-prints, 1207.4211, Jul. 2012.

Conference Presentations

1 F. Trang, H. Rogalla, and Z. Popović, "Resonant Response of High Temperature Superconducting Split-Ring Resonators",
Applied Superconductivity Conference, Portland, OR., Oct. 2012.

2 F. Trang, E. F. Kuester, H. Rogalla, and Z. Popović, "Fabrication Sensitivity of Double-Sided Split-Ring Resonator Arrays",
USNC-URSI, Boulder, CO., Jan. 2012.